



Effect of HVOF Process Parameters on TiO₂ Coatings: An Approach Using DoE and First-Order Process Maps

G. A. Clavijo-Mejía^{1,2} · D. G. Espinosa-Arbeláez³ · J. A. Hermann-Muñoz¹ · A. L. Giraldo-Betancur⁴ · J. Muñoz-Saldaña¹

Submitted: 11 April 2019 / in revised form: 15 July 2019 / Published online: 24 July 2019
© ASM International 2019

Abstract High-velocity oxy-fuel deposition stages of titanium oxide coatings were analyzed and reported here. For the first stages of deposition, process maps were used to evaluate the influence of deposition parameters such as stand-off distance (SOD), powder feed rate (PFR) and fuel/oxygen ratio (F/O) on velocity and temperature of in-flight particles. These parameters were then combined with particle size distribution (PSD) to further optimize the deposition process considering the spray trace width and the area covered by splats and non-molten particles as responses. Furthermore, the structural, morphological and mechanical characteristics either of single splats, clusters of semi- and/or non-molten particles or coatings were obtained by, x-ray diffraction, Raman spectroscopy, scanning electron microscopy and nanoindentation. During coating build-up, lower PFR and F/O induce more splat particles and fewer clusters of semi- and/or non-molten particles, whereas the PSD affects the width of the spray trace. The combination of F/O and SOD upper levels was related to a high percentage of TiO₂ splat deposition. Finally, the proposed methodology allowed to obtain dense

TiO₂ coatings with a higher content of rutile phase and an average thickness of 65 μm.

Keywords Design of experiments · HVOF · Thermal spray · TiO₂ coatings

Introduction

Titanium oxide (TiO₂) is one of the most investigated ceramics due to its excellent properties in different applications, such as photocatalysis, photoelectric devices, hydrogen production, biomedical and corrosion protection (Ref 1). As a coating, it is used to protect or to enhance adherence (as a bond coat- *BC*) of the subsequent layers. Among the techniques that have been reported to obtain this kind of coatings are sol-gel, electrophoretic deposition, dip and spin coating, thermal spray techniques (Ref 2-4). TiO₂ coatings deposited by thermal spray (TS) have been studied either as a single layer (Ref 5-7) or as a *BC* enhancing the adherence of topcoats (TC) with metallic surfaces (Ref 8-11). Among the different TS technologies, high-velocity oxygen fuel (HVOF) has demonstrated to enhance the adherence and the crack propagation, stress, and abrasion resistance of these coatings (Ref 12-14).

During the HVOF process, the in-flight particles impacting the substrate are flattened and solidified in different shapes and sizes seeking to form disk-like shapes or splats, which are the desired basic unit in the coating build-up process. Additionally, other effects are observed upon the impact of in-flight particles such as the formation of clusters of semi- and/or non-molten particles, splashing, rebounding, or imprints due to the projection of non-molten particles (Ref 15, 16).

✉ J. Muñoz-Saldaña
jmunoz@cinvestav.mx

¹ Centro de Investigación y de Estudios Avanzados del IPN, Lib. Norponiente 2000, Fracc. Real de Juriquilla, 76230 Querétaro, Qro., Mexico

² Institute of Research for Ceramics-IR CER, UMR 7315, CNRS, Centre Européen de la Céramique (CEC), Université de Limoges, 12 Rue Atlantis, 87068 Limoges Cedex, France

³ Center of Engineering and Industrial Development, CIDESI, Av. Pie de la Cuesta No. 702, 76125 Querétaro, Qro., Mexico

⁴ CONACYT-Centro de Investigación y de Estudios Avanzados del IPN, Lib. Norponiente 2000, Fracc. Real de Juriquilla, 76230 Querétaro, Qro., Mexico

The splats and coatings characteristics such as morphology, adherence, chemical composition, microstructure, etc., are defined by the combination of TS deposition parameters: stand-off distance (SOD), powder feed rate (PFR), fuel/oxygen (F/O) ratio, number of passes (NOP), particle size distribution (PSD), total gas flow, among others. From these parameters, the F/O, SOD, PFR, and PSD are known to have an influence on the particle velocity and temperature and thus coating quality (Ref 17–21). A methodology based on a combination of process maps and design of experiments (DoE) that includes the analysis of variance (ANOVA) has been reported, where temperature and velocity of in-flight particles are linked with TS parameters giving significant information about the deposition process and its relation with the final coating characteristics (Ref 22–25).

TS parameters for the TiO₂ coating fabrication has been already analyzed by DoE (Ref 26, 27). However, there are no contributions to the analysis of the TiO₂ HVOF deposition with the combination of process maps and DoE, neither for the first stages of splat formation or for the coating build-up.

In this work, the different stages of TiO₂ deposition process by HVOF were addressed: firstly, by studying the influence of F/O, PFR, and SOD on velocity and temperature of the in-flight particles using first-order process maps. Secondly, by analyzing the significance of these parameters in combination with feedstock PSD and their effects on the first stages of coating deposition, including splats characteristics, covered area, and the width of spray trace footprint. Finally, the outcomes of this analysis were applied to deposit high-quality TiO₂ coatings.

Experimental Methods

Materials and Spraying Process

Fused and crushed TiO₂ powder with 99% of purity (Metco 102, Oerlikon Metco, USA) was used as feedstock. Two PSD were studied during the experimentation: *as-received* ($d_{10} = 15.5 \mu\text{m}$, $d_{50} = 25.6 \mu\text{m}$, and $d_{90} = 39.4 \mu\text{m}$) and after sieving passing through 500 mesh ($d_{10} = 9.0 \mu\text{m}$, $d_{50} = 17.9 \mu\text{m}$, and $d_{90} = 27.5 \mu\text{m}$). 301 stainless steel plate samples (SS301) with $1.0 \times 1.0 \times 0.3 \text{ cm}$ were used as substrates. Before the spraying process, the substrates were grit blasted with alumina and heated at 300 °C (Ref 28). A DJ2700-hybrid HVOF gun (Sultzer-Metco, USA) was manipulated with a 6-axis robot (KUKA, GmbH, Germany). Propane and nitrogen were used as fuel and powder carrier gas, respectively. Details of TiO₂ spray conditions for the in-flight particle temperature and velocity analysis and splat fabrication are given in Tables 1 and 2. All experiments

Table 1 Parameters combination used in the velocity and temperature analysis

Condition	PFR, g/min	SOD, cm	F/O
C1	12	15	0.14
C2	24	15	0.14
C3	24	30	0.14
C4	12	30	0.14
C5	12	30	0.27
C6	24	30	0.27
C7	24	15	0.27
C8	12	15	0.27

Table 2 Parameters combination used in the splat fabrication analysis

Condition	PFR, g/min	SOD, cm	F/O
R1	15	18	0.21
R2	20	18	0.21
R3	20	25	0.21
R4	15	25	0.21
R5	15	25	0.27
R6	20	25	0.27
R7	20	18	0.27
R8	15	18	0.27

were performed at a constant total gas flow of 627 LPM. The F/O ratio was calculated based on Eq 1 (Ref 20).

$$\gamma = \frac{\text{fuel flow}}{(\text{Oxygen flow} + 0.21 \text{ air flow})} \tag{Eq 1}$$

Velocity and Temperature Measurement and Analysis

The velocity and temperature measurements of the in-flight particle were performed using the G3C AccuraSpray system (Tecnar, Canada). The F/O, SOD, and PFR were used as variables for a 2³ factorial DoE. The higher and lower values for each parameter were chosen based on previous reports and the operating limits of the HVOF system (Ref 20, 29–31). The TiO₂ powder (*as-received*) was sprayed under the parameters presented in Table 1 to construct first-order process maps. The ANOVA was done to predict the parameter combination to reach temperature of in-flight particles close to the TiO₂ melting point (~ 1855 °C) (Ref 32) and highest possible velocity to avoid splashing effects.

Splat Fabrication and Analysis

A reduced 2^3 factorial DoE was selected around the statistically predicted results in the previous analysis. The combination of parameters is listed in Table 2. The studied parameters were the SOD, PFR, F/O, and PSD of the feedstock powder. The TiO_2 powder was sprayed onto mirror-polished substrates ($2.5 \times 2.5 \times 0.3$ cm) by a single spray pass.

Coatings Fabrication

TiO_2 coatings were fabricated on SS301 grit-blasted substrates after 10 passes (NOP = 10) by using the combination of parameters selected from the *splat fabrication and analysis*. Samples were deposited using the *as-received* and *sieved* powder. Coatings were metallographically prepared to analyze their cross sections by SEM.

Characterization and Analysis

PSD of TiO_2 powders in the *as-received* and *sieved* conditions was measured by a HELOS/BR laser diffractometer (Sympatec, GmbH, Germany). Measurements were performed using a RODOS method for dry powder with air pressurized at 0.2 bar. The morphology of the feedstock powder, splats, and clusters of semi- and/or non-molten particles, as well as cross-sectional coatings microstructure, was studied using SEM (XL30, ESEM-Philips) at 10 kV electron acceleration voltage and a secondary electron (SE) detector. Structural characterization was performed on the TiO_2 feedstock powder and coatings using a DMax 2100 x-ray diffractometer (Rigaku, Japan) with monochromatic $\text{CuK}\alpha$ radiation ($\lambda = 1.5406 \text{ \AA}$) operated at 30 kV and 20 mA. The XRD patterns were recorded between 20° and 70° on a 2θ scale, with a step size of 0.02° , a counting time of 0.5 s and at 5° incidence angle. The formation of TiO_2 splats and clusters of semi- and/or non-molten particles formation was evaluated by TH4-100 optical microscopy (OM) (Olympus, Japan) and XL30 scanning electron microscopy (SEM) (Philips, Netherlands). The percentage of the covered area was analyzed using image processing with ImageJ[®] software. The spray trace width was also measured and reported. The elastic modulus (E) and hardness (H) of deposits at the first stages were obtained using an Ubi-1 nanoindenter (Hysitron, USA) and a diamond Berkovich tip. The maximum load was $500 \mu\text{N}$ in a partial loading test with 5 cycles to assure uniformity of the contact conditions with the different deposits. The number of indents was variable depending on the available tested deposits. The results were evaluated following the Oliver and Pharr method (Ref 33). Furthermore, Raman spectra of the feedstock powder

and the first particles deposited on the substrate were recorded with a micro-Raman spectrometer LabRam HR-800 (Horiba Jobin-Yvon, Japan) with a He-Ne laser ($= 632.8 \text{ nm}$) of 20 mW incident power and $1 \mu\text{m}$ spot size. All spectra were normalized to the intensity of the 420 cm^{-1} band. The obtained results allowed to feed the DoE and subsequently, an ANOVA of the reduced 2^3 experimental design was performed to predict the combination of parameters. The final goal is to obtain higher splat formation events and reduce the number of clusters of semi- and/or non-molten particles seeking to fabricate a wider spray trace.

Results and Discussion

Feedstock Powder Characteristics

Figure 1 shows the SEM micrographs (Fig. 1a and c) and cumulative particle size distribution (Fig. 1b and d) of the feedstock (TiO_2 Metco 102) for *as-received* and *sieved* powder, respectively. The powder morphology is irregular with flat faces and pronounced corners at the edges, which is expected due to its fabrication process (Fig. 1a and c). Figure 1(b) and (d) shows the reduction of particle size distribution after the sieving process. The 90% of the cumulative distribution of the particles was measured with a maximum size of $39.4 \mu\text{m}$ for *as-received* powder (Fig. 1b) and $27.5 \mu\text{m}$ for the *sieved* sample (Fig. 1d). Geometry and size distribution of particles are relevant because of their effect on the coating build-up due to their interaction with the gas flow during the HVOF process (Ref 34, 35). It has been reported that the feedstock characteristics have a direct influence on the coating properties, such as porosity, thickness, adherence, among others (Ref 14, 36). However, to the author's knowledge, no reports are available describing the influence of the PSD on the first stages of deposition of TiO_2 coatings by HVOF.

Therefore, feedstock characteristics together with other process parameters described above have a direct influence on the velocity and temperature of the in-flight particles, which in turn will impact the properties of the HVOF TiO_2 splats and coatings (Ref 37).

Velocity and Temperature Analysis

The influence of the parameter's combination on the velocity and temperature of in-flight particles was evaluated using first-order process maps (Fig. 2). Figure 2(a) shows the selected parameter combinations that include SOD, F/O, and PFR. As a result, velocity and temperature of the in-flight particles for a SOD = 30 cm are in the range of 580–720 m/s and 1485–1496 °C,

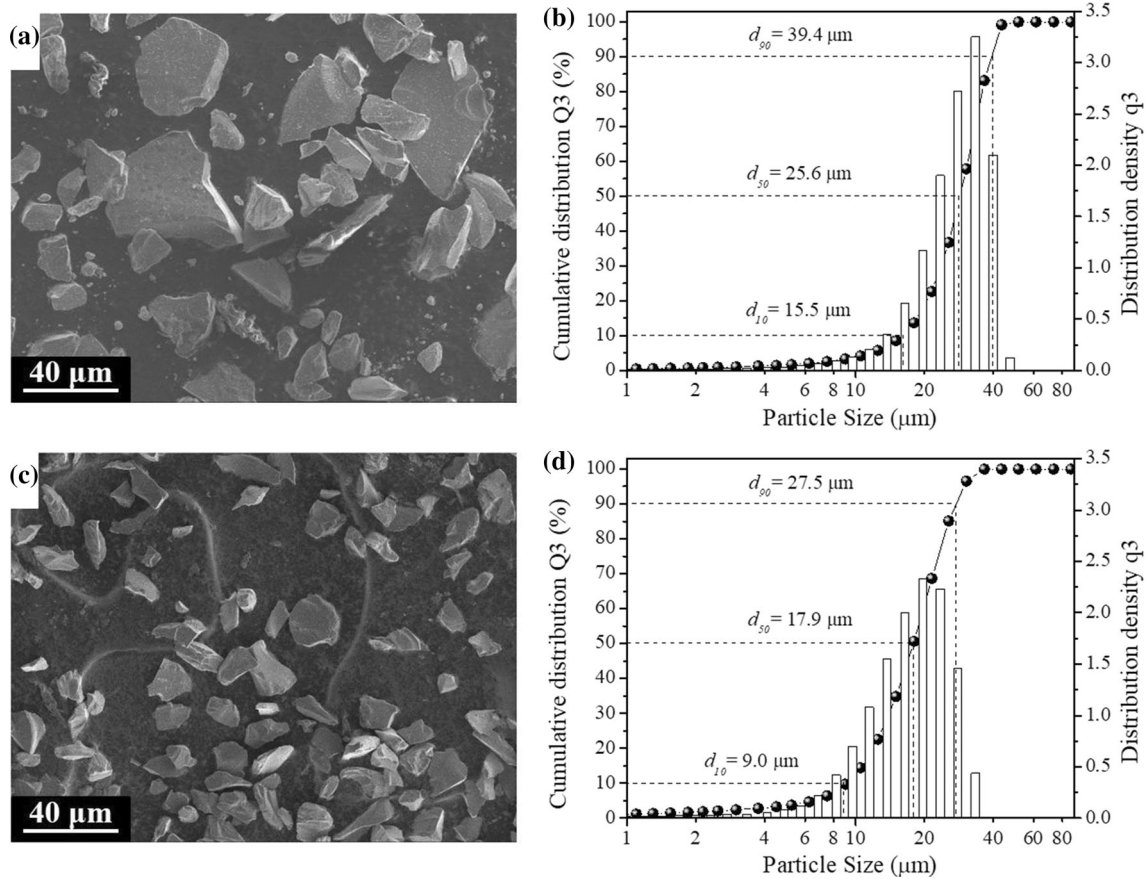


Fig. 1 Typical SEM micrographs and cumulative particle size distribution of (a, b) as-received TiO₂ powder and (c, d) sieved powder

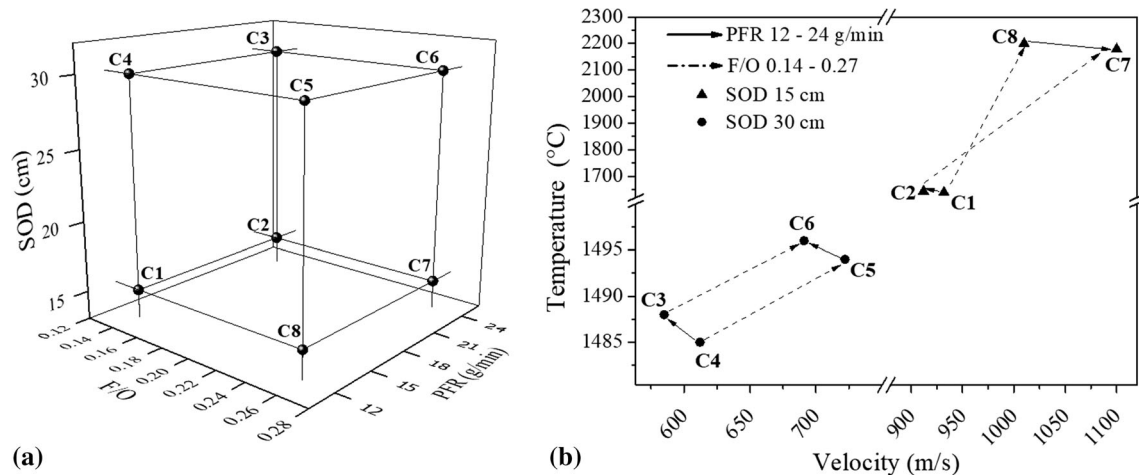


Fig. 2 Two-level factorial design and its corresponding first-order process map using powder in as-received conditions. (a) selected parameters and levels, (b) particle velocity and temperature variations from C3, C4, C5, C6 and C1, C2, C7, C8 experiments, respectively

respectively (Fig. 2b). Reducing SOD to 15 cm, the velocity and temperature increased to 910–1100 m/s and 1650–2200 °C (Fig. 2b). Furthermore, the velocity and temperature of the particles increased with higher F/O ratio in both working SOD (15 and 30 cm) (Fig. 2b). F/O ratio increments affect the combustion reaction within the

entrance chamber, increasing the gas temperature and velocity and in consequence, the correspondent momentum and temperature of in-flight particles (Ref 38). This behavior has been reported elsewhere for Al₂O₃ coatings obtained by HVOF, where velocity and temperature of the particles increased by 100 m/s and 150 °C, respectively,

for F/O going from 0.15 to 0.27 (Ref 39). PFR had no significant effect on the particle temperature and velocity except for C7 and C8 combination of parameters, where the particle velocity decreased with lower PFR. Moreover, the velocity and temperature decreased as expected with higher SOD values, as a result of the kinetic energy loss due to the reduction of the gas drag force over the particles and the air counterforce in the HVOF process (Ref 40, 41).

If the residence time of the particle in the flame is enough to melt and complete the droplet formation, a too high impact velocity of the particle will generate instabilities during the splat flattening and in consequence splashing (Ref 42). Based on this and the results obtained from the first-order map, an ANOVA was performed to predict the parameter's combination seeking an in-flight particle temperature close to the melting point of rutile TiO_2 (~ 1855 °C) and the highest attainable velocity to avoid splashing effects.

The obtained parameter combination was $\text{SOD} = 21.87$ cm, $\text{PFR} = 20.36$ g/min and $\text{F/O} = 0.239$. A reduced two-level factorial design of experiment around this parameter combination was established (Fig. 3a) and its parameters are presented in Table 2. Figure 3b shows the corresponding process map. The obtained velocity and temperature of the in-flight particles deposited under the new proposed sets of parameters were between 738–937 m/s and 1515–1960 °C. The influence of the SOD and F/O on the in-flight particle characteristics agrees with the previous first-order process maps analysis (Fig. 2b).

A complementary experimental evaluation was undertaken using *as-received* TiO_2 powders at fixed PFR and F/O parameters and is shown in Fig. 4, in which velocity and temperature evolution as a function of the SOD were evaluated. The velocity and temperature of the particles dropped by 300 m/s and 140 °C by increasing the SOD

showing a linear (Adj. $R^2 = 0.971$) and an exponential (Adj. $R^2 = 0.991$) trend, respectively.

The used diagnostic measurement is based on the G3C AccuraSpray system ensemble measurement method. This system measures the average of particles temperature and does not distinguish between individual particles (Ref 43). Despite the lack of information regarding the shape or width of the particle temperature distribution by using the ensemble technique, the measurement accuracy of the AccuraSpray system compared to single-particle methods has been demonstrated (Ref 44). Moreover, the ensemble method is insensitive to the movement of the spray pattern, it can be used for heavily loaded HVOF processes (Ref 45) and the time of response is shorter than in other techniques (Ref 46). Hence, considering the mentioned facts, the study of the influence of the parameter's combination on the relative in-flight particle velocity and temperature using the G3C AccuraSpray diagnostic system can be regarded as reliable.

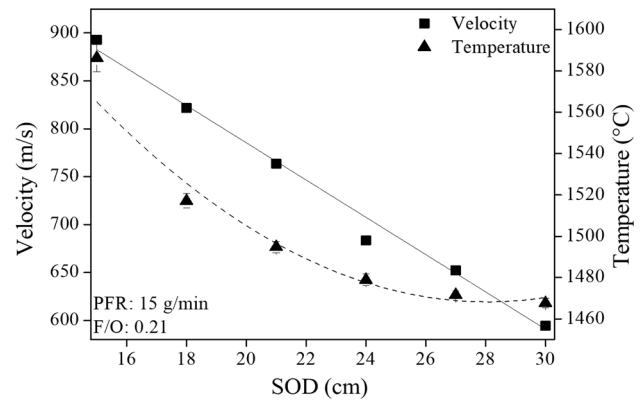


Fig. 4 Stand-off distance effect on the velocity and temperature of TiO_2 particles of as-received powder

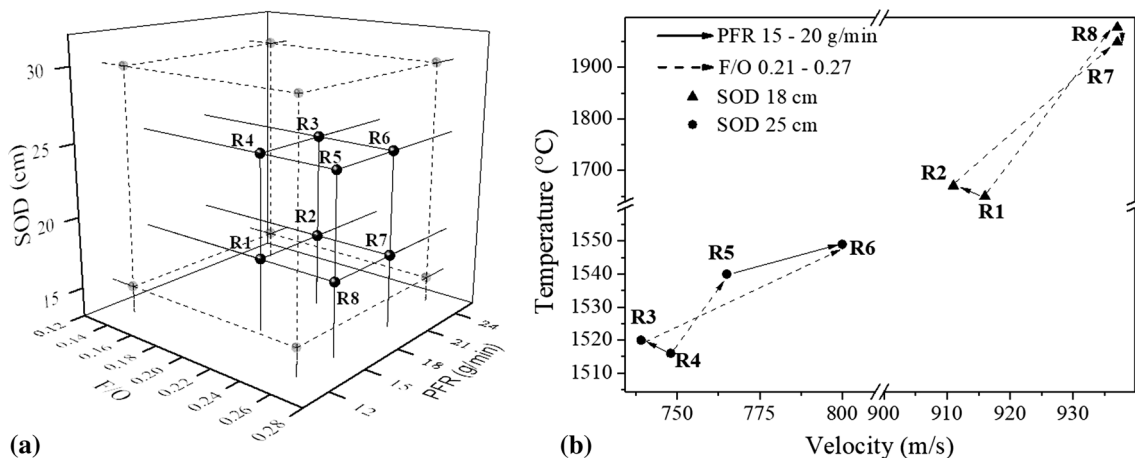


Fig. 3 Reduced factorial design and its corresponding first-order process map using in as-received, (a) selected parameters and levels, (b) particle velocity and temperature variations from R3, R4, R5, R6 and R1, R2, R7, R8 experiments, respectively

Splat Fabrication and Analysis

From the reduced two-level factorial design of experiments, the R4 and R8 spray conditions show the combination of the lower and higher velocities and temperatures of the in-flight particles, 748 m/s-1516 °C and 937 m/s-1977 °C, respectively. Optical micrographs at two magnifications of the first impacted and deposited particles using the *as-received* feedstock powder under R4 and R8 parameters combinations are presented in Fig. 5. A higher fraction of disk-like splats is noted using R4 (Fig. 5a) compared to R8 condition (Fig. 5c). Higher magnification micrographs allow seeing a more significant splashing effect and the presence of small melted particles or sub-splats (Ref 42) under R8 (Fig. 5b) in contrast to R4 (Fig. 5d). This is a consequence of a combination of high-velocity and high-temperature conditions from the in-flight particles. Thus, considering the morphology, size, and occupied area of splats, the R4 parameter combination was selected for further analysis of the first stages of deposition.

SEM micrographs at different magnifications of impacted particles during the first stages of deposition with both PSD are shown in Fig. 6 evidencing the formation of

deposits with a different melting degree. The PSD of the feedstock powder shows a clear effect on the deposits type. For instance, for the R4 condition, the *as-received* powder confirms a higher combination of molten (smaller ones) semi-molten and non-molten (bigger ones) deposits, resulting in splashing and clusters of semi- and/or non-molten particles (Fig. 6a and b). In contrast, under the same deposition conditions, the *sieved* powders lead to a higher density of splat-shaped deposits (Fig. 6c and d).

The nature of these first deposits can be identified comparing their mechanical properties with those of the TiO₂ in bulk form. The nanoindentation analysis of the deposits is shown in Fig. 7. A typical AFM micrograph from clusters of semi- and/or non-molten particles, splats, and substrate (zones 1, 2, 3, respectively) is presented in Fig. 7(a). The inset from same Fig. 7(a) reveals the splat profile and a thickness of about 290 nm. The nanoindentation tests were carried out on the mentioned zones, and the correspondent force-displacement graphs are shown in Fig. 7(b). This type of indentation test was chosen to assure right contact conditions with different deposits. For the 500 μN tests, the penetration depth was higher in the clusters of semi- and/or non-molten particles compared to results

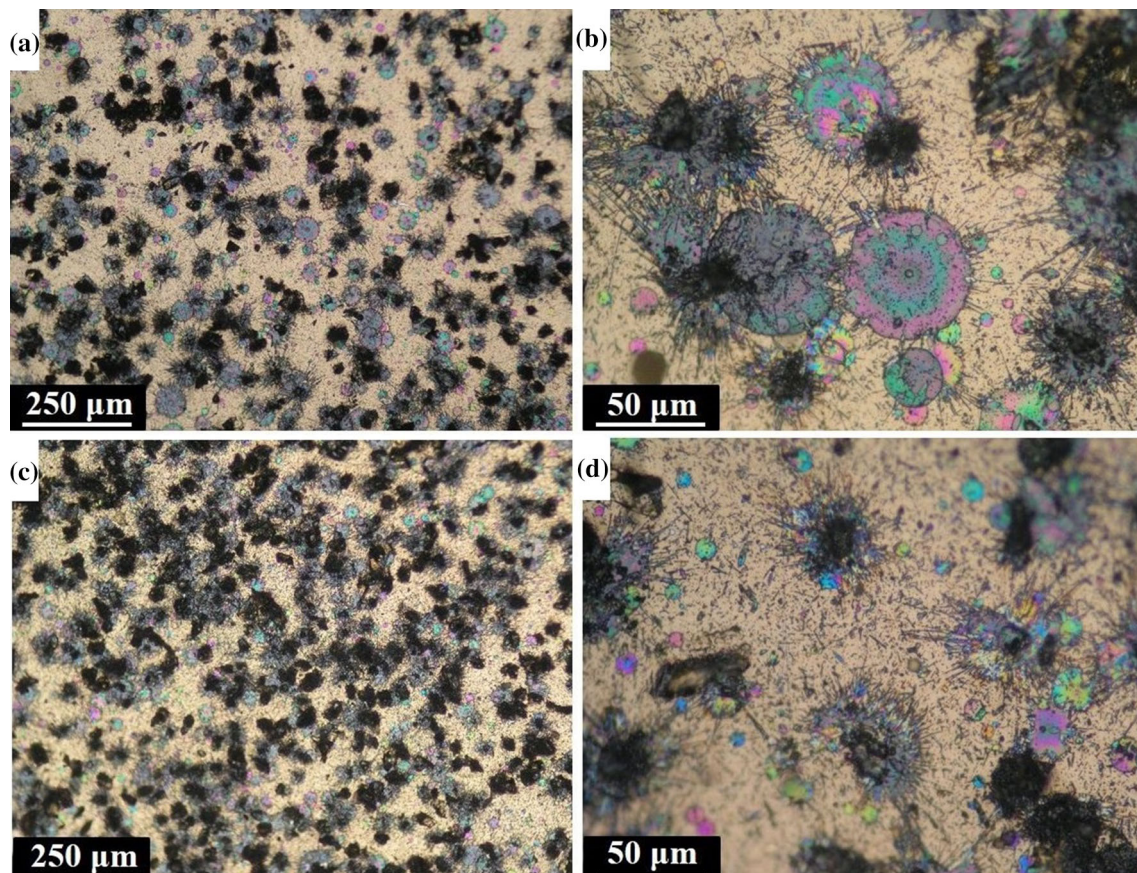


Fig. 5 Optical micrographs of first deposits under (a) R4 parameters combination at $10\times$, (b) R4 parameters combination at $50\times$, (c) R8 parameters combination at $10\times$ and (d) R8 parameters combination at $50\times$

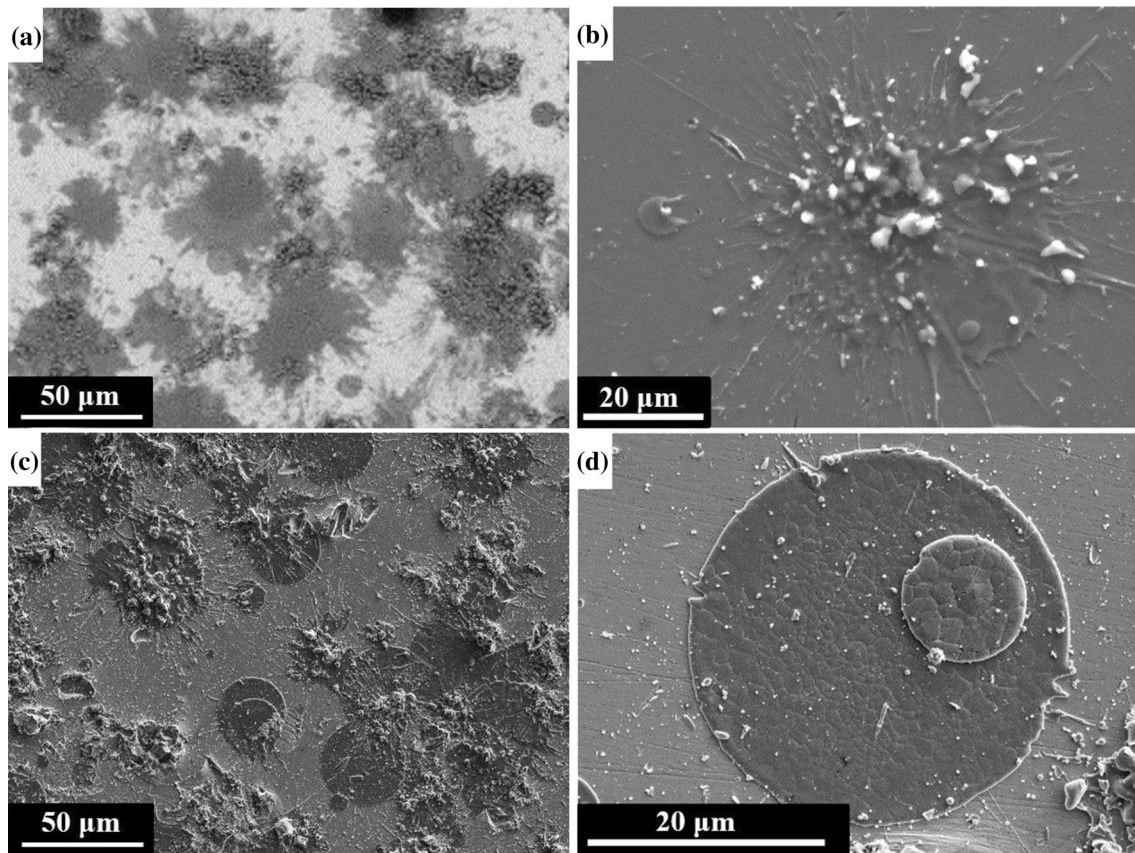


Fig. 6 SEM micrographs showing different types of deposits under R4 parameter condition using as-received (a, b) and sieved (c, d) feedstock powders

obtained for splats and substrate. It is clear that clusters of semi- and/or non-molten particles are TiO_2 adhered particles with poor cohesion as a result of non-molten or semi-molten conditions. The Young modulus, E was calculated from the reduced elastic modulus using $\nu = 0.30$ (Ref 47) as a Poisson ratio of TiO_2 of rutile. For the diamond tip, the Poisson ratio and E are reported elsewhere ($\nu_i = 0.07$ and $E_i = 1141$ GPa) (Ref 48). Figure 7(c) and (d) shows the Weibull distribution analysis to represent the E and H of clusters of semi- and/or non-molten particles, splats, and the substrate. The low $E = 80.9$ GPa of partial clusters of semi- and/or non-molten particles is because they collapse under low indentation loads, exhibiting their poor cohesion, which typically leads to further coating delamination and poor mechanical properties. The measured E for the stainless steel substrate was 235.6 GPa, which matches the expected value (Ref 49).

The mechanical properties of a TiO_2 splat ($E = 176.6$ GPa and $H = 11.0$ GPa) were obtained from Weibull analysis and are similar to those reported in previous results for plasma sprayed TiO_2 coatings ($E = 163.5 \pm 22.4$ – 232.7 ± 21.2 and $H = 7.6 \pm 2$ – 11.9 ± 1.1) (Ref 50). The wide range of values reported by

Ctibor et al. is attributed to the presence of different predominant crystal orientations (Ref 50). The measured Young modulus of the splat was 62.61% lower than rutile bulk TiO_2 (282 GPa) (Ref 29). The reason for the difference in mechanical properties between TiO_2 coatings and bulk lies in the influence of the limited degree of contact between splats or between the splat and substrates (Ref 51).

To confirm the structural characteristics of splats and clusters of semi- and/or non-molten particles, analysis of micro-Raman spectra was undertaken. The results are compared to the feedstock powder (TiO_2 Metco 102) and shown in Fig. 8. The Raman spectrum of the TiO_2 Metco 102 powder exhibits bands at 150 and 262 and 429 and 608 cm^{-1} , which are related to the presence of anatase and rutile phases, respectively (Ref 52, 53). For the clusters of semi- and/or non-molten particles (1) vibrational bands at 144, 252, 418 and 602 cm^{-1} were identified, which are slightly shifted from those detected in the feedstock powder (associated with rutile and anatase phases) due to transformations during the deposition process. No other significant structural changes were observed in clusters of semi- and/or non-molten particles compared to feedstock powder. Finally, the Raman spectrum of a single splat (2)

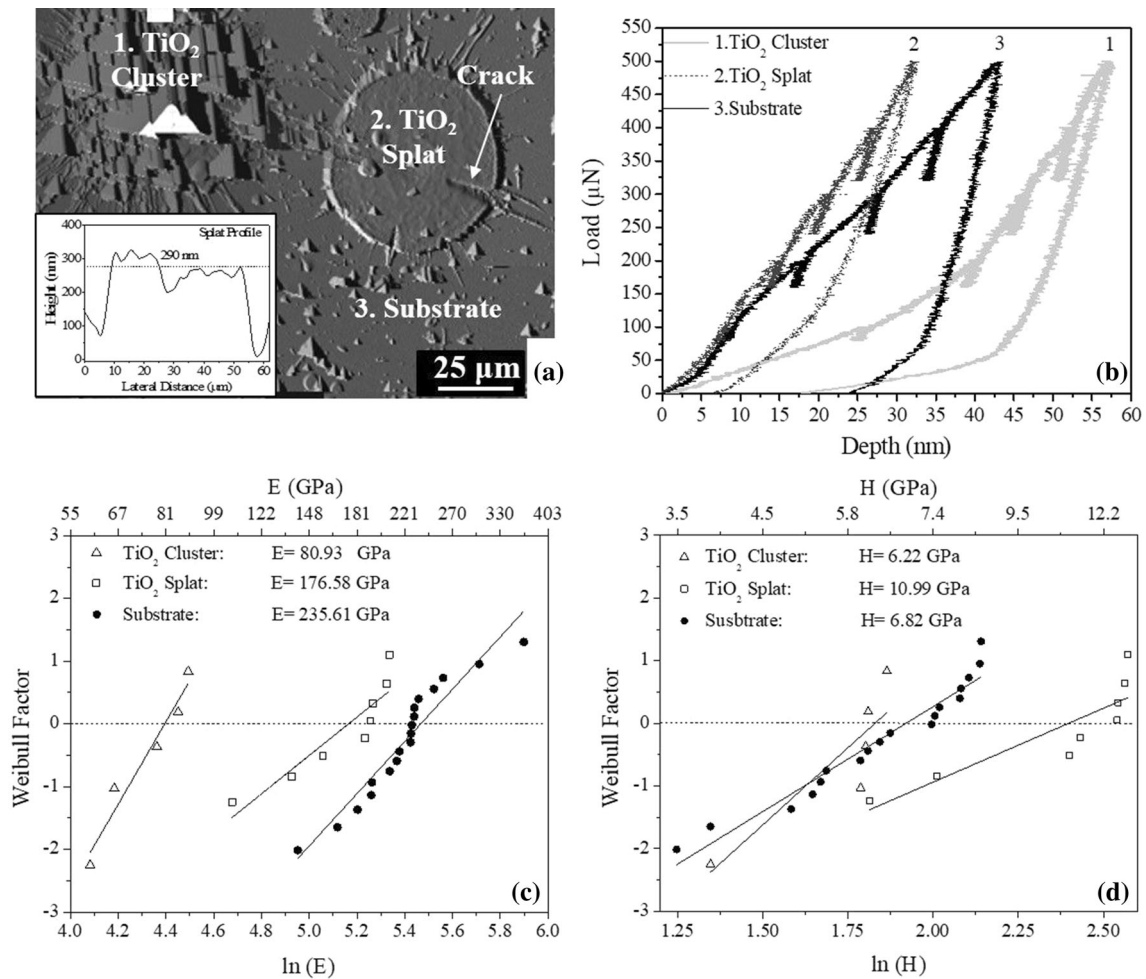
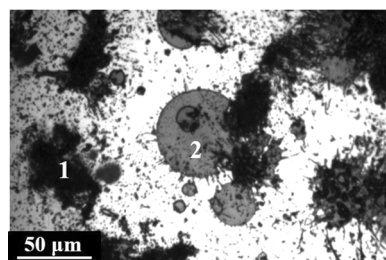


Fig. 7 Identification of TiO₂ deposits on the basis of their mechanical properties measured by nanoindentation. (a) AFM micrograph showing the type of TiO₂ deposits. An inset of the splat surface profile

is included. (b) Load–displacement curves, Weibull distribution analysis of (c) elastic modulus and (d) hardness are also shown

Fig. 8 Typical micro-Raman spectra of TiO₂ feedstock powder, cluster of semi- and/or non-molten particles and splat



shows bands at 427 and 602 cm⁻¹, which are unambiguously attributed to a rutile phase (Ref 53) and a complete vanishing of the anatase bands located around 150 and 260 cm⁻¹.

Again, the lower Young modulus of a rutile phase splat than rutile bulk titania (282 GPa) (Ref 29) is surprising. It has been argued elsewhere that the mechanical behavior of coatings is affected by the degree of contact between splats and might also

apply to single splats and the substrate (Ref 54). Flattening and solidification, as well as their relation with the contact degree of a droplet impacting a surface, have been discussed based on experimental and theoretical approaches (Ref 19, 55, 56). Impacted molten or semi-molten particles with a different distribution of temperature across their volume transfer heat to the substrate during flattening and solidification, leading to the formation of splash deposits, homogenous splats or deposits with a heterogeneous semi-molten state (Ref 57, 58). The splat morphology depends on different variables such as the Reynolds (Re) number and melting index (MI) of the impacted particle which have a direct influence on splat flattening, solidification, and fragmentation (Ref 59), and surface cracking (Ref 60). Re and MI are part of a group of different parameters which need to be further studied to understand TiO_2 splat formation and semi-molten heterogeneity. In this contribution, heterogeneous flattening of TiO_2 splats is well noted in the micrograph in Fig. 5(b), where the splats present different concentrically color rings given by light diffraction. Moreover, cracks are present in the splat surface as is shown in Fig. 7(a). Splat heterogeneity in flattening and solidification suggests a correlation with the low splat mechanical properties compared to bulk TiO_2 , however other analyses are still needed to fully explain this relation.

Nevertheless, TiO_2 clusters from semi- and/or non-molten deposits are mainly responsible for poor coating's quality, low mechanical properties, low adherence, inter-layer delamination, among others. Additionally, for the first stages of deposition, the characteristics of the spray trace strongly define the deposition quality.

Figure 9 shows the SOD, PFR, F/O and PSD effect on the spray trace and the percentage of splats and clusters of semi- and/or non-molten particles in the covered area after a multiple response optimization in the DoE. The following statements can be drawn from this figure.

- Variations in SOD, PFR, and F/O show no significant changes in the spray trace width (Fig. 9a, b, and c, respectively).
- In contrast, the most remarkable influence on the spray trace width is the PSD parameter. Spray trace was 3 mm broader at low values of this parameter (Fig. 9d). Smaller particles will get a higher surface temperature avoiding particles bouncing upon impact on the substrate, improving the deposition efficiency (Ref 61). There is a direct relation between splat impacting temperature and the deposition efficiency.
- All the parameters had a considerable effect on the percentage of the splats-covered area (Fig. 9). This response variable is increased at high SOD values (Fig. 9a) as well as setting low values of PFR, F/O, and PSD.

- Rising the F/O from 0.18 to 0.27 and SOD from 18 to 25 cm leads to an increase in the percentage of clusters of semi- and/or non-molten particles by 1 and 1.2%, respectively (Fig. 9a and c). Moreover, higher PFR values at the same HVOF conditions increase the number of such deposits (Fig. 9b).
- PSD has a higher influence on the percentage of clusters of semi and/or non-molten particles percentage than SOD, PFR, and F/O (Fig. 9). The clusters-covered area was 3.7% higher using the R4 condition with sieved compared to the as-received TiO_2 feedstock powder. This change seems to be related to the particle velocity and temperature using sieved powder (Fig. 3); however, the clusters and splat percentage increase after increasing the deposition efficiency by using a finer feedstock powder.

Thus, the R4 combination of parameters using sieved powder (high SOD, low PFR, and F/O) showed such values of velocity and temperatures, where most of the projected TiO_2 particles were heated and accelerated to be properly flattened seeking to decrease splashing effects.

The predicted combination of parameters by ANOVA to increase the splat percentage and spray width trace and to decrease the number of clusters of semi- and/or non-molten particles is shown in Table 3.

Coatings Fabrication and Analysis

Figure 10 presents the SEM cross-sectional micrographs of TiO_2 coatings deposited under R4 condition, using both feedstock powders (*as-received* and *sieved* powder conditions). Figure 10(a) shows a non-uniform thin coating (2–35 μm) (1), (2) obtained with the *as-received* powder, which is related to the low amount of splats formed during the first stages of deposition. This finding was predicted from the analysis performed above. On the contrary, the coating fabricated under the same condition but using a *sieved* powder presents a uniform and denser morphology, as it can be seen in Fig. 10(b). The cross-sectional image shows a thicker coating (54–72 μm) (1) with more continuous interface with the metallic substrate (2). The present analysis led to obtaining a coating with such morphological characteristics; hence, the adopted methodology was suitable to enhance the quality of TiO_2 thermal spray coatings by HVOF. Finally, Fig. 11 presents the XRD patterns of the feedstock powder and the two studied coatings. The XRD pattern of the feedstock presents different phases of titanium oxide, namely anatase (PDF # 98-001-1631) and rutile (PDF # 98-001-7742), as it was stated in the micro-Raman analysis. Furthermore, Magneli phases with a Ti_xO_{2x-1} stoichiometry were also detected with XRD analysis. After the coating build-up,

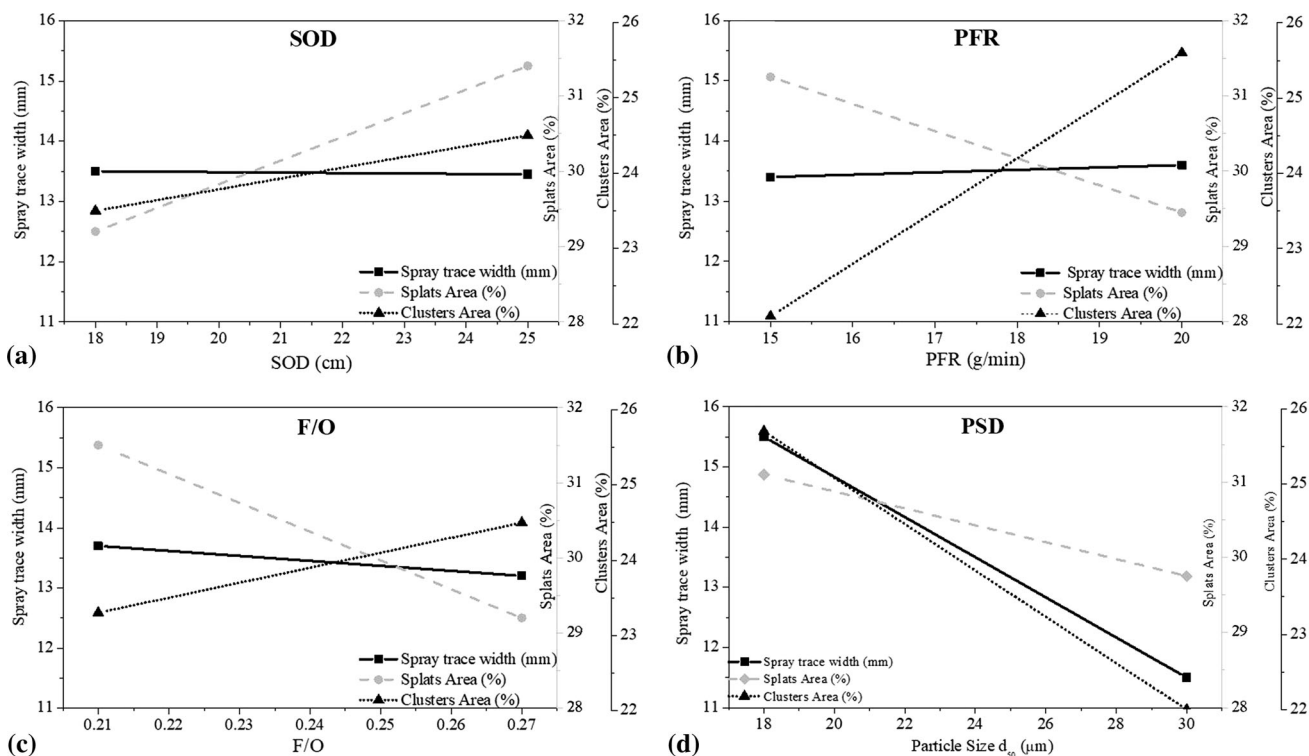


Fig. 9 Effect of (a) SOD, (b) PFR, (c) F/O ratio and (d) PSD on the spray trace width in a single pass, as well as filtering area of splats and TiO₂ clusters of semi- and/or non-molten particles

Table 3 Statistical prediction of HVOF parameters combination to obtain first coating stages with maximum values of splats, first-pass width and minimum values of clusters of semi- and/or non-molten particles

Statistical prediction		Predicted response value		
Parameter	Value	Spray trace width (mm)	Splats (%)	Clusters of semi- and/or non-molten particles (%)
SOD, cm	25	12	30	19
PFR, g/min	15			
F/O	0.21			
PSD, μm	< 38.63			

rutile phase content was increased while Magneli and anatase phases decrease because of the high-temperature exposition during the thermal spray process. Likewise, the diffractogram for the coating obtained using R4 combination and *as-received* powder conditions presents more peaks of Magneli phases around 35 and 43° 2θ than the one fabricated with *sieved* powder under R4 conditions. Therefore, the TiO₂ coating obtained with R4 parameter combination and using *sieved* powder allows obtaining a higher content of rutile phase within its structure.

Conclusions

- The optimized processing parameters to reach in-flight particle temperature and velocity (1855 °C and 800 m/

s) conditions to promote splat formation with *as-received* powder were F/O= 0.23, SOD= 21.87 cm and PFR= 20.36 g/min.

- Increasing F/O ratio (0.15 to 0.27) directly affects the velocity and temperature of the in-flight particles for both types of feedstock powders. On the contrary, SOD increments (15 to 30 cm) showed a decreasing tendency in the particle velocity and temperature. Moreover, the percentage of splats in the first deposition stages increases considerably by reducing the F/O ratio at high SOD values. Therefore, the particles that remain for a longer time within the process flame will adopt a proper physical state, generating a greater number of splats in the first deposition stages. Additionally, higher PFR values produced more clusters of semi- and/or non-molten particles adhered to the substrate in the first

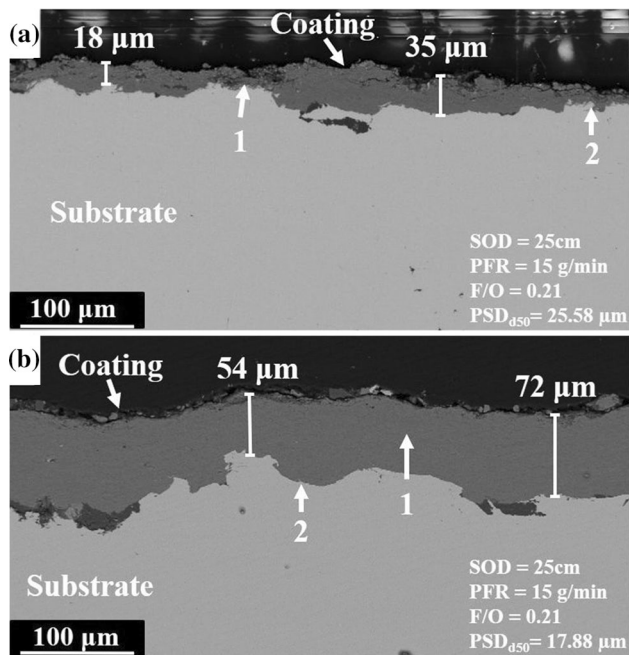


Fig. 10 SEM micrographs from the cross sections of TiO₂ coatings deposited under conditions R4 using (a) as-received and (b) sieved powder

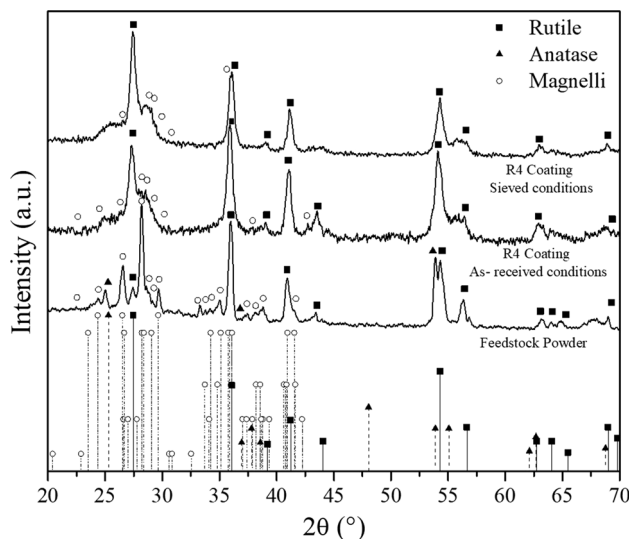


Fig. 11 X-ray diffraction patterns of the powder and R4 coatings using as-received and sieved powder conditions

stages of TiO₂ deposition. Finally, reducing the PSD directly improved the splat formation and morphology and increased the width of spray trace.

- Nanoindentation and Raman analysis allowed to identify the nature of the different deposits. For instance, a single splat exhibited mechanical properties ($E = 176.6$ GPa and $H = 11$ GPa) close to thermally sprayed TiO₂ coatings in Rutile phase, which was confirmed by micro-Raman analysis. Clusters of semi- and/or non-

molten particles showed lower values ($E = 80.9$ GPa and $H = 6.2$ GPa) and a combination of phases.

- The use of the parameter combination: SOD= 25 cm, PFR= 15 g/min, F/O= 0.21 and *as-received* feedstock powder (PSD $d_{50} = 25.6$ μm) leads to obtain a poor and non-uniform coating as well as major amounts of Magneli phases within its structure. On the contrary, TiO₂ coatings deposited under the same parameters and using *sieved* powder (PSD $d_{50} = 17.9$ μm) presented a dense uniform microstructure and consist mainly of rutile phase. This experimental parameter combination was close to the predicted in the ANOVA analysis which will allow generating coatings with higher splats percentage (29.9%), lower percentage of clusters of semi- and/or non-molten particles (19%) and a higher spray trace width (12 mm) (SOD= 25 cm, PFR= 15 g/min, F/O= 0.21 and PSD of *sieved* powder).
- The methodology proposed in this contribution leads to the fabrication of dense and uniform TiO₂ coatings by HVOF thermal spray with a mainly rutile structure and thickness of 65 ± 7 μm.

Acknowledgements The authors thank CONACYT for the master and Ph.D. financial support and to the Catedras program. This Project Was Funded by CONACYT 232612, 272095, 279738, and 293429, 881 projects and carried out partially at CENAPROT and LIDTRA national laboratories. Authors also thank Carlos Poblano, Alma Gabriela Mora, Jose Eleazar Urbina-Alvarez and Adair Jimenez-Nieto for the technical support.

References

1. U. Diebold, The Surface Science of Titanium Dioxide, *Surf. Sci. Rep.*, 2003, **48**(5-8), p 53-229. [https://doi.org/10.1016/S0167-5729\(02\)00100-0](https://doi.org/10.1016/S0167-5729(02)00100-0)
2. T. Kemmitt, N.I. Al-Salim, M. Waterland, V.J. Kennedy, and A. Markwitz, Photocatalytic Titania Coatings, *Curr. Appl. Phys.*, 2004, **4**(2-4), p 189-192. <https://doi.org/10.1016/j.cap.2003.11.006>
3. A.R. Boccaccini, M. Rossetti, J.A. Roether, S.H. Sharif Zein, and M. Ferraris, Development of Titania Coatings on Glass Foams, *Constr. Build. Mater.*, 2009, **23**(7), p 2554-2558. <https://doi.org/10.1016/j.conbuildmat.2009.02.019>
4. M.J. Santillán, N. Quaranta, F. Membrives, J.A. Roether, and A.R. Boccaccini, Processing and Characterization of Biocompatible Titania Coatings by Electrophoretic Deposition, *Key Eng. Mater.*, 2009, **412**, p 189-194
5. Y.-P. Lu, M.-S. Li, S.-T. Li, Z.-G. Wang, and R.-F. Zhu, Plasma-Sprayed Hydroxyapatite + Titania Composite Bond Coat for Hydroxyapatite Coating on Titanium Substrate, *Biomaterials*, 2004, **25**(18), p 4393-4403. <https://doi.org/10.1016/j.biomater.2003.10.09>
6. M.G. Latorre, *Recubrimientos Biocompatibles Obtenidos Por Proyección Térmica y Estudio in Vitro de La Función Osteoblástica*, Universitat de Barcelona, Barcelona, 2007
7. R. Tomaszek, L. Pawlowski, L. Gengembre, J. Laureyns, and A. Le Maguer, Microstructure of Suspension Plasma Sprayed Multilayer Coatings of Hydroxyapatite and Titanium Oxide, *Surf.*

- Coatings Technol.*, 2007, **201**(16-17), p 7432-7440. <https://doi.org/10.1016/j.surfcoat.2007.02.013>
8. R.B. Heimann, Design of Novel Plasma Sprayed Hydroxyapatite-Bond Coat Bioceramic Systems, *J. Therm. Spray Technol.*, 1999, **8**(4), p 597-604. <https://doi.org/10.1361/105996399770350304>
 9. G. Goller, The Effect of Bond Coat on Mechanical Properties of Plasma Sprayed Bioglass-Titanium Coatings, *Ceram. Int.*, 2004, **30**(3), p 351-355. [https://doi.org/10.1016/S0272-8842\(03\)00107-X](https://doi.org/10.1016/S0272-8842(03)00107-X)
 10. F.N. Oktar, M. Yetmez, S. Agathopoulos, T.M.L. Goerne, G. Goller, I. Ipeker, and J.M.F. Ferreira, Bond-Coating in Plasma-Sprayed Calcium-Phosphate Coatings, *J. Mater. Sci. Mater. Med.*, 2006, **17**(11), p 1161-1171. <https://doi.org/10.1007/s10856-006-0544-5>
 11. H. Kurzweg, R.B. Heimann, T. Troczynski, and M.L. Wayman, Development of Plasma-Sprayed Bioceramic Coatings with Bond Coats Based on Titania and Zirconia, *Biomaterials*, 1998, **19**(16), p 1507-1511. [https://doi.org/10.1016/S0142-9612\(98\)00067-2](https://doi.org/10.1016/S0142-9612(98)00067-2)
 12. B. Jeffery, M. Pepler, R.S. Lima, and A. McDonald, Bactericidal Effects of HVOF-Sprayed Nanostructured TiO₂ on Pseudomonas Aeruginosa, *J. Therm. Spray Technol.*, 2009, **19**(1-2), p 344-349. <https://doi.org/10.1007/s11666-009-9369-3>
 13. H. Melero, J. Fernández, S. Dosta, and J.M. Guilemany, Caracterización de Nuevos Recubrimientos Biocompatibles de Hidroxiapatita-TiO₂ Obtenidos Mediante Proyección Térmica de Alta Velocidad, *Boletín la Soc. Española Cerámica y Vidr.*, 2011, **50**(2), p 59-64. <https://doi.org/10.3989/cyv.082011>
 14. R.S. Lima and B.R. Marple, From APS to HVOF Spraying of Conventional and Nanostructured Titania Feedstock Powders: A Study on the Enhancement of the Mechanical Properties, *Surf. Coatings Technol.*, 2006, **200**(11), p 3428-3437. <https://doi.org/10.1016/j.surfcoat.2004.10.137>
 15. S. Chandra and P. Fauchais, Formation of Solid Splats during Thermal Spray Deposition, *J. Therm. Spray Technol.*, 2009, **18**(2), p 148-180. <https://doi.org/10.1007/s11666-009-9294-5>
 16. P. Bansal, P.H. Shipway, and S.B. Leen, Effect of Particle Impact on Residual Stress Development in HVOF Sprayed Coatings, *Proc. Int. Therm. Spray Conf.*, 2006, **15**(December), p 570-575. <https://doi.org/10.1361/105996306X146703>
 17. A.N.N. Sakakibara, H. Tsulcudá, The Splat Morphology of Plasma Sprayed Particle and the Relation to Coating Property, in *Thermal Spray 2000: Surface Engineering via Applied Research* (2000), p 753-758 (6)
 18. P. Fauchais, M. Fukumoto, A. Vardelle, and M. Vardelle, Knowledge Concerning Splat Formation: An Invited Review, *J. Therm. Spray Technol.*, 2004, **13**(3), p 337-360. <https://doi.org/10.1361/10599630419670>
 19. M. Pasandideh-Fard, V. Pershin, S. Chandra, and J. Mostaghimi, Splat Shapes in a Thermal Spray Coating Process: Simulations and Experiments, *J. Therm. Spray Technol.*, 2002, **11**(2), p 206-217. <https://doi.org/10.1361/105996302770348862>
 20. H. Ruiz-Luna, D. Lozano-Mandujano, J.M. Alvarado-Orozco, A. Valarezo, C.A. Poblano-Salas, L.G. Trápaga-Martínez, F.J. Espinoza-Beltrán, and J. Muñoz-Saldaña, Effect of HVOF Processing Parameters on the Properties of NiCoCrAlY Coatings by Design of Experiments, *J. Therm. Spray Technol.*, 2014, **23**(6), p 950-961. <https://doi.org/10.1007/s11666-014-0121-2>
 21. D. Cheng, Q. Xu, G. Trapaga, and E.J. Lavernia, The Effect of Particle Size and Morphology on the In-Flight, *Metall. Mater. Trans. B*, 2001, **32**(June), p 525-535. <https://doi.org/10.1007/s11663-001-0037-3>
 22. M. Friis and C. Persson, Control of Thermal Spray Processes by Means of Process Maps and Process Windows, *J. Therm. Spray Technol.*, 2003, **12**(1), p 44-52. <https://doi.org/10.1361/105996303770348492>
 23. A. Valarezo, W.B. Choi, W. Chi, A. Gouldstone, and S. Sampath, Process Control and Characterization of NiCr Coatings by HVOF-DJ2700 System: A Process Map Approach, *J. Therm. Spray Technol.*, 2010, **19**(5), p 852-865. <https://doi.org/10.1007/s11666-010-9492-1>
 24. C. Pierlot, L. Pawlowski, M. Bigan, and P. Chagnon, Design of Experiments in Thermal Spraying: A Review, *Surf. Coat. Technol.*, 2008, **202**(18), p 4483-4490. <https://doi.org/10.1016/j.surfcoat.2008.04.031>
 25. S. Hasan and J. Stokes, Design of Experiment Analysis of the Sulzer Metco DJ High Velocity Oxy-Fuel Coating of Hydroxyapatite for Orthopedic Applications, *J. Therm. Spray Technol.*, 2010, **20**(1-2), p 186-194. <https://doi.org/10.1007/s11666-010-9566-0>
 26. S.M. Forghani, M.J. Ghazali, A. Muchtar, A.R. Daud, N.H.N. Yusoff, and C.H. Azhari, Effects of Plasma Spray Parameters on TiO₂-Coated Mild Steel Using Design of Experiment (DoE) Approach, *Ceram. Int.*, 2013, **39**(3), p 3121-3127. <https://doi.org/10.1016/j.ceramint.2012.09.092>
 27. M. Gardon, J.M. Guilemany, The Influence of Titanium Sub-Oxides in Thermal Sprayed Coatings, in *Proceedings International Thermal Spray Conference, 2012* (May 2012)
 28. M. Lufitha, *Effect of Substrate Temperature on Coating Adhesion*, University of Toronto, Toronto, 2001
 29. R.S. Lima and B.R. Marple, Optimized HVOF Titania Coatings, *J. Therm.*, 2003, **12**(September), p 360-369. <https://doi.org/10.1361/105996303770348230>
 30. Y. Liu, T.E. Fischer, and A. Dent, Comparison of HVOF and Plasma-Sprayed Alumina/Titania Coatings—Microstructure, Mechanical Properties and Abrasion Behavior, *Surf. Coat. Technol.*, 2003, **167**(1), p 68-76. [https://doi.org/10.1016/S0257-8972\(02\)00890-3](https://doi.org/10.1016/S0257-8972(02)00890-3)
 31. R.S. Lima and B.R. Marple, High Weibull Modulus HVOF Titania Coatings, *J. Therm. Spray Technol.*, 2003, **12**(June), p 240-249. <https://doi.org/10.1361/105996303770348357>
 32. D.L. Perry and S.L. Phillips, *Handbook of Inorganic Compounds*, CRC Press LLC, Boca Raton, 1995
 33. W.C. Oliver and G.M. Pharr, An Improved Technique for Determining Hardness and Elastic Modulus Using Load and Displacement Sensing Indentation Experiments, *J. Mater. Res.*, 1992, **7**(6), p 1564-1583
 34. P. Fauchais, G. Montavon, and G. Bertrand, From Powders to Thermally Sprayed Coatings, *J. Therm. Spray Technol.*, 2010, **19**(January), p 56-80. <https://doi.org/10.1007/s11666-009-9435-x>
 35. O.C. Brandt, Mechanical Properties of HVOF Coatings, *J. Therm. Spray Technol.*, 1995, **4**(June), p 147-152. <https://doi.org/10.1007/BF02646105>
 36. M. Gardon and J.M. Guilemany, Milestones in Functional Titanium Dioxide Thermal Spray Coatings: A Review, *J. Therm. Spray Technol.*, 2014, **23**(April), p 577-595. <https://doi.org/10.1007/s11666-014-0066-5>
 37. M. Gaona, R.S. Lima, and B.R. Marple, Influence of Particle Temperature and Velocity on the Microstructure and Mechanical Behaviour of High Velocity Oxy-Fuel (HVOF)-Sprayed Nanostructured Titania Coatings, *J. Mater. Process. Technol.*, 2008, **198**(1-3), p 426-435. <https://doi.org/10.1016/j.jmatprotec.2007.07.024>
 38. M. Li, D. Shi, and P.D. Christofides, Modeling and Control of HVOF Thermal Spray Processing of WC-Co Coatings, *Powder Technol.*, 2005, **156**(2-3), p 177-194. <https://doi.org/10.1016/j.powtec.2005.04.011>
 39. E. Turunen, T. Varis, S.P. Hannula, A. Vaidya, A. Kulkarni, J. Gutleber, S. Sampath, and H. Herman, On the Role of Particle State and Deposition Procedure on Mechanical, Tribological and Dielectric Response of High Velocity Oxy-Fuel Sprayed Alumina

- Coatings, *Mater. Sci. Eng., A*, 2006, **415**(1-2), p 1-11. <https://doi.org/10.1016/j.msea.2005.08.226>
40. K. Aik, J. Cizek, K.A. Khor, and I. Dlouhy, In-Flight Temperature and Velocity of Powder Particles of Plasma-Sprayed TiO₂, *J. Therm. Spray Technol.*, 2013, **22**(8), p 1320-1327. <https://doi.org/10.1007/s11666-013-9993-9>
 41. A.G.M. Pukaszewicz, H.E. de Boer, G.B. Sucharski, R.F. Vaz, and L.A.J. Procopiak, The Influence of HVOF Spraying Parameters on the Microstructure, Residual Stress and Cavitation Resistance of FeMnCrSi Coatings, *Surf. Coat. Technol.*, 2017, **327**, p 158-166. <https://doi.org/10.1016/j.surfcoat.2017.07.073>
 42. J.A. Hermann-Muñoz, J.A. Rincón-López, G.A. Clavijo-Mejía, A.L. Giraldo-Betancur, J.M. Alvarado-Orozco, A. De Vizcaya-Ruiz, and J. Muñoz-Saldaña, Influence of HVOF Parameters on HAp Coating Generation: An Integrated Approach Using Process Maps, *Surf. Coat. Technol.*, 2019, **358**, p 299-307. <https://doi.org/10.1016/j.surfcoat.2018.11.029>
 43. G. Mauer, R. Vaben, and D. Stöver, Comparison and Applications of DPV-2000 and Accuraspray-G3 Diagnostic Systems, *J. Therm. Spray Technol.*, 2007, **16**(September), p 414-424. <https://doi.org/10.1007/s11666-007-9047-2>
 44. P. Fauchais and A.M. Vardelle, Sensors in Spray Processes, *J. Therm. Spray Technol.*, 2014, **19**(4), p 668-694. <https://doi.org/10.1007/s11666-010-9485-0>
 45. J.R. Fincke, D.C. Haggard, and W.D. Swank, Particle Temperature Measurement in the Thermal Spray Process, *J. Therm. Spray Technol.*, 2001, **10**, p 255-266. <https://doi.org/10.1361/105996301770349358>
 46. C. Moreau, J. Bisson, R.S. Lima, and B.R. Marple, Diagnostics for Advanced Materials Processing by Plasma Spraying, *Pure Appl. Chem.*, 2005, **77**(2), p 443-462. <https://doi.org/10.1351/pac200577020443>
 47. J.W. Jr., W. Tefft, and D.L. Jr., Elastic Constants of Rutile (TiO₂), *J. Res. Nat. Bur. Stand.*, 1962, **66**(6), p 465-471. <https://doi.org/10.6028/jres.066A.047>
 48. G.M. Pharr and W.C. Oliver, Measurement of Thin Film Mechanical Properties Using Nanoindentation, *MRS Bull.*, 1992, **17**(7), p 28-33. <https://doi.org/10.1557/S0883769400041634>
 49. J.R. Davis, *ASM Specialty Handbook® Stainless Steels*, Materials Park, ASM International, 1994, p 584
 50. P. Ctibor, P. Boháč, M. Stranyánek, and R. Čtvrtlík, Structure and Mechanical Properties of Plasma Sprayed Coatings of Titania and Alumina, *J. Eur. Ceram. Soc.*, 2006, **26**(16), p 3509-3514. <https://doi.org/10.1016/j.jeurceramsoc.2005.12.018>
 51. L. Pawlowski, *The Science and Engineering of Thermal Spray Coatings*, 2nd ed., Wiley, Hoboken, 2008
 52. R. Tomaszek, L. Pawlowski, L. Gengembre, J. Laureyns, Z. Znamirowski, and J. Zdanowski, Microstructural Characterization of Plasma Sprayed TiO₂ Functional Coating with Gradient of Crystal Grain Size, *Surf. Coat. Technol.*, 2006, **201**(1-2), p 45-56. <https://doi.org/10.1016/j.surfcoat.2005.10.033>
 53. I.N. Martyanov, T. Berger, O. Diwald, S. Rodrigues, and K.J. Klabunde, Enhancement of TiO₂ Visible Light Photoactivity through Accumulation of Defects during Reduction–Oxidation Treatment, *J. Photochem. Photobiol. A Chem.*, 2010, **212**(2-3), p 135-141. <https://doi.org/10.1016/j.jphotochem.2010.04.006>
 54. V.V. Sobolev and J.M. Guilemany, Flattening of Droplets and Formation of Splats in Thermal Spraying: A Review of Recent Work—Part 2, *J. Therm. Spray Technol.*, 1999, **8**(1), p 87-101. <https://doi.org/10.1361/105996399770350610>
 55. M. Vardelle, A. Vardelle, A.C. Leger, P. Fauchais, and D. Gobin, Influence of Particle Parameters at Impact on Splat Formation and Solidification in Plasma Spraying Processes, *J. Therm. Spray Technol.*, 1994, **4**(March), p 50-58. <https://doi.org/10.1007/BF02648528>
 56. H. Fukunuma, R. Huang, Y. Tanaka, and Y. Uesugi, Mathematical Modeling and Numerical Simulation of Splat Cooling in Plasma Spray Coatings, *J. Therm. Spray Technol.*, 2009, **18**(December), p 965-974. <https://doi.org/10.1007/s11666-009-9366-6>
 57. Z. Zhu, K. Spyros, and S. Gu, Numerical Study of Molten and Semi-Molten Ceramic Impingement by Using Coupled Eulerian and Lagrangian Method, *Acta Mater.*, 2015, **90**(March), p 77-87. <https://doi.org/10.1016/j.actamat.2015.02.010>
 58. M. Bertagnolli, M. Marchese, G. Jacucci, S.D. Ioannis, and S. Noeltling, Thermomechanical Simulation of the Splashing of Ceramic Droplets on a Rigid Substrate, *J. Comput. Phys.*, 1997, **133**(2), p 205-221. <https://doi.org/10.1006/jcph.1996.5468>
 59. L. Li, A. Vaidya, S. Sampath, H. Xiong, and L. Zheng, Particle Characterization and Splat Formation of Plasma Sprayed Zirconia, *J. Therm. Spray Technol.*, 2006, **15**(March), p 97-105. <https://doi.org/10.1361/105996306X92668>
 60. K. Yang, M. Liu, K. Zhou, and C. Deng, Recent Developments in the Research of Splat Formation Process in Thermal Spraying, *J. Mater.*, 2013, **2013**, p 1-14
 61. T. Itsukaichi, S. Osawa, and R. Ahmed, Influence of Powder Size and Strength on HVOF Spraying—Mapping the Onset of Spitting, in *Thermal Spray 2003 Advanced Science Application Technology* (2003), p 819-824.

Publisher's Note Springer Nature remains neutral with regard to jurisdictional claims in published maps and institutional affiliations.